CMOS compatible novel plasmonic refractive index sensor with high sensitivity based on alternative plasmonic material

MD. OMAR FARUQUE[*], RABIUL AL MAHMUD, RAKIBUL HASAN SAGOR
Department of Electrical and Electronic Engineering, Islamic University of Technology (IUT), Gazipur 1704, Bangladesh

A plasmonic refractive index (RI) sensor based on a highly doped silicon waveguide is proposed and investigated numerically. The RI sensor utilizes a heavily doped silicon waveguide instead of a conventional metal-insulator-metal (MIM) waveguide which makes it complementary metal-oxide-semiconductor (CMOS) compatible. A ring waveguide is coupled with the straight waveguide like MIM ring resonator structures and a similar resonance phenomenon is observed. The sensitivity is investigated and a sensitivity of 2150 nm/RIU is realized. The plasmonic sensor consists of a simple framework and uses only silicon waveguide and does not require any special material which makes it suitable for sensing systems in integrated optical circuits and also suitable for nanofabrication since it is CMOS compatible.

1. Introduction

The Surface Plasmon Polaritons (SPPs) are infrared or visible frequency electromagnetic waves that travel along with a metal-dielectric interface [1]. Utilizing this mechanism of SPP propagation along with the metal-dielectric interface, several plasmonic devices have been investigated to date which includes plasmonic filters [2]–[4], couplers [5]–[7], splitters [8]–[10], sensors [11]–[13], etc. Among the plasmonic devices, plasmonic sensors have drawn a lot of attention due to their smaller size along with high sensitivity which makes them suitable for integrated optical systems [14]. Most of the plasmonic sensors are based on metal-insulator-metal waveguide along with a resonator which uses different resonance phenomenon and thus act as different kinds of sensors such as refractive index sensors [12], [13], [15], temperature sensors [15]–[17], gas sensors [18], [19], biosensors [10], [20], [21], etc. As the metal of the MIM structure, gold and silver are the most used metals and the air is the most common insulator [10]–[13], [15]–[17].

Though metal-insulator-metal (MIM) waveguides use silver or gold due to their small ohmic losses and ability to confine light within considerable propagation length [22], they suffer another loss mechanism namely interband transitions at optical frequencies [23]. The imaginary part of the permittivity is mainly responsible for this loss. Thus most of the applications require the imaginary part of the metal's dielectric permittivity to be small. However, in conventional plasmonic materials i.e. metals, the carrier concentration is very high (10^{23} cm^{-3}) and this increases the magnitude of the imaginary part of the permittivity. Another issue is the large magnitude of

the real part of the permittivity in metals which causes several challenges as most of the plasmonic devices require meta-materials with a nearly balanced polarization response [24], [25]. Both of the above-mentioned problems would be minimized to a great extent if the carrier concentrations in metals could be reduced. But the carrier concentrations of natural metals like gold and silver are almost fixed. Besides loss and not adjustable dielectric permittivity, nanofabrication of metals grown as thin films also gives rise to some problems. The optical properties of metal films degrade significantly compared to bulk metals [26], [27]. Thus fabrication of metal films maintaining their optical properties is a challenge and would require some special efforts.

To overcome the above-mentioned drawbacks of natural metals, some alternative materials can be used which will have a similar behavior like metals. The optical properties of metals are mainly described by their dielectric permittivity, ε, and magnetic permeability, μ [28]. At optical frequencies, the magnetic permeability for metal is almost close to unity. Thus their optical response is mainly characterized by their dielectric permittivity, ε. The real part of the permittivity describes the polarization response and the imaginary part is responsible for optical losses [29]. At optical frequency, metals exhibit negative real permittivity compared to the positive real permittivity of dielectrics [30]. Considering each of the factors mentioned above, highly doped p-silicon is used as an alternative plasmonic material that shows similar properties of metals after a particular doping concentration and also allows SPP propagation. Its carrier concentration can be varied which makes its dielectric permittivity adjustable. This allows the minimization of

loss mechanisms in plasmonic materials. From the fabrication point of view, silicon photonics has been recognized as a key technology in recent times [31]–[39]. One of the main advantages of silicon photonics is that it is CMOS compatible.

Though researchers have proposed several sensors with high sensitivity [9]–[11], [15], [40], most of them used gold or silver as a plasmonic material that is not

CMOS compatible. The plasmonic sensor reported here uses only highly doped silicon as a plasmonic material which makes it completely CMOS compatible.

In this paper, we investigated a plasmonic sensor that is based on a highly doped silicon waveguide coupled with a ring resonator where the air is used as the insulator of the straight waveguide and the material under sense will fill the cavity in the ring resonator. However, instead of the metals like gold or silver which are not CMOS compatible, a highly doped p-silicon is used here which possesses a negative real permittivity after a certain doping concentration, and as a result, it behaves like metals. Moreover, the design proposed here consists of a very simple framework that is easier to fabricate. Besides, no other materials like graphene, vanadium oxide, indium tin oxide, or metals need to be deposited which makes the fabrication process much simpler [41]. According to our investigation, the plasmonic sensor has a sensitivity as high as 2150 nm/RIU and can detect change as small as 0.005. The size of the sensor is also smaller and compared to the other plasmonic or hybrid plasmonic sensors. But the main contribution of this paper is to design a sensor using a doped silicon waveguide instead of a traditional MIM waveguide which provides an easier way of fabrication using CMOS technology.

2. Theoretical model and device design

The p-silicon used here must be doped up to a certain carrier concentration to make it behave like a metal. For our design, it is assumed to be doped in the range of 10^{20} to 10^{21} cm^{-3}. Carrier concentration in this range has been practically shown by Shahzad et al. [42], Linaschke et al. [43], Mizushima et al. [44], Vina et al.[45], Ma et al.[46], Miyao et al. [47] and Jellison Jr et al. [48]. The highest carrier concentration of $2×10^{22}$ cm^{-3} in Silicon has been reported by Nobili et al [49]. The complex relative permittivity of highly doped silicon can be described by the Lorentz-Drude model [14].

$$\varepsilon(\omega) = \varepsilon_\infty - \frac{\omega_p^2}{\omega^2\left(1+i\dfrac{1}{\omega\tau}\right)}$$

(1)

If the real part and imaginary parts are separated, (1) becomes,

$$\varepsilon(\omega) = \left(\varepsilon_\infty - \frac{\omega_p^2\tau^2}{1+\omega^2\tau^2}\right) + i\frac{\omega_p^2\tau}{\omega\left(1+\omega^2\tau^2\right)}$$

(2)

where ω_p is the plasma frequency, ε_∞ is the infinite frequency relative permittivity or the background permittivity, τ is the electron/hole relaxation time, $\omega = \dfrac{2\pi c}{\lambda}$ is the angular frequency, c is the speed of light in vacuum and i is the imaginary unit. In the case of the highly doped degenerate intrinsic semiconductors $\omega_p^2 = \dfrac{Ne^2}{\varepsilon_0 m_{eff}}$ and $\tau = \dfrac{\mu m_{eff}}{e}$ where, N is the free carrier concentration, μ is the electron/hole's drift mobility and m_{eff} is the averaged electron/hole effective mass [41]. Usually, the angular frequency $\omega >> \omega_p$ and $\omega\tau >> 1$ [50]. Thus equation 1 can be rewritten as,

$$\varepsilon(\omega) = \left(\varepsilon_\infty - \frac{\sigma}{\omega^2\varepsilon_0\tau}\right) + i\frac{\sigma}{\omega^3\tau^2\varepsilon_0}$$

(3)

where, $\sigma = eN\mu$ is the conductivity of the doped silicon and e is the charge of an electron and ε_0 is the free space permittivity. The infinite frequency relative permittivity or the background permittivity is the high-frequency limiting value that is approximately 11.7 for silicon and is independent of the doping concentration [29], [51]. Here, $\mu = 50$ [52] and $m_{eff} = 0.37*m_0$, where, m_0 is the mass of the electron [53]. The real part of the complex permittivity becomes negative after a certain concentration which can be calculated using equation (2). This phenomenon has been experimentally demonstrated by Shahzad et al. [42]. Comparison between the values calculated from equation (2) and the experimental value for carrier concentration of $6×10^{19}$ cm^{-3} and $1×10^{20}$ cm^{-3} has been shown in Figs. 1(a) and 1(b) respectively. The values have been found very close to each other for smaller wavelengths. Although it shows some error for larger wavelengths, this work is done for much smaller wavelengths where the error is very small. Thus the theoretical modeling is verified.

From both the experimental and theoretical results, it has been observed that the dependence of permittivity on both the wavelength and doping concentration is almost linear. The real and imaginary parts of relative permittivity of highly doped silicon against the doping concentration and wavelength are shown in Figs. 2(a), 2(b), 2(c) and 2(d) respectively.
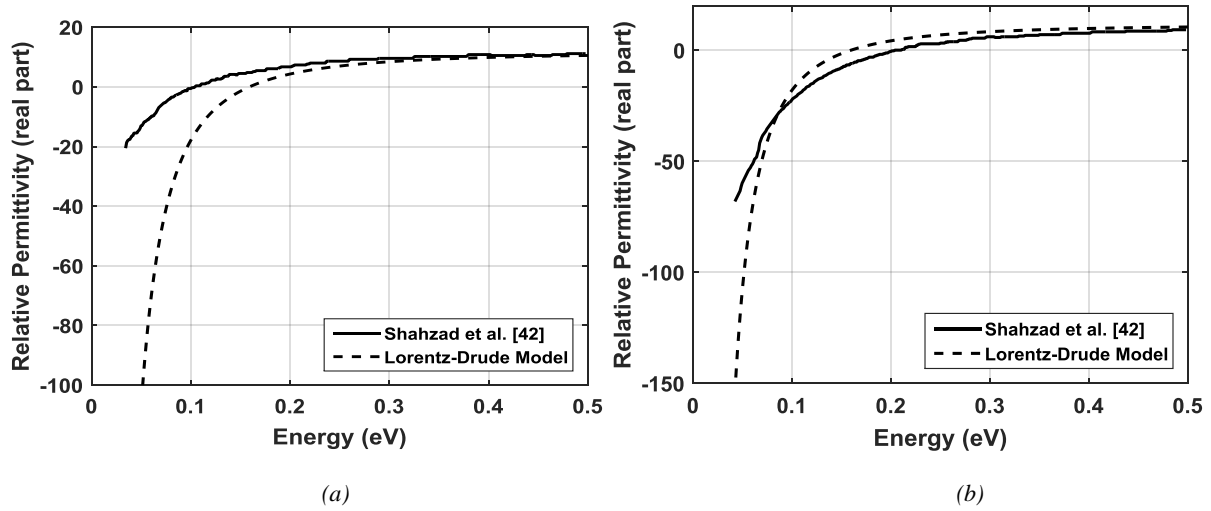
(a)

(b)

Fig.1. Comparison of the real parts of the permittivity between theoretical value and experimental value for carrier concentration of (a) 6×10^{19} cm^{-3} (b) 1×10^{20} cm^{-3}.
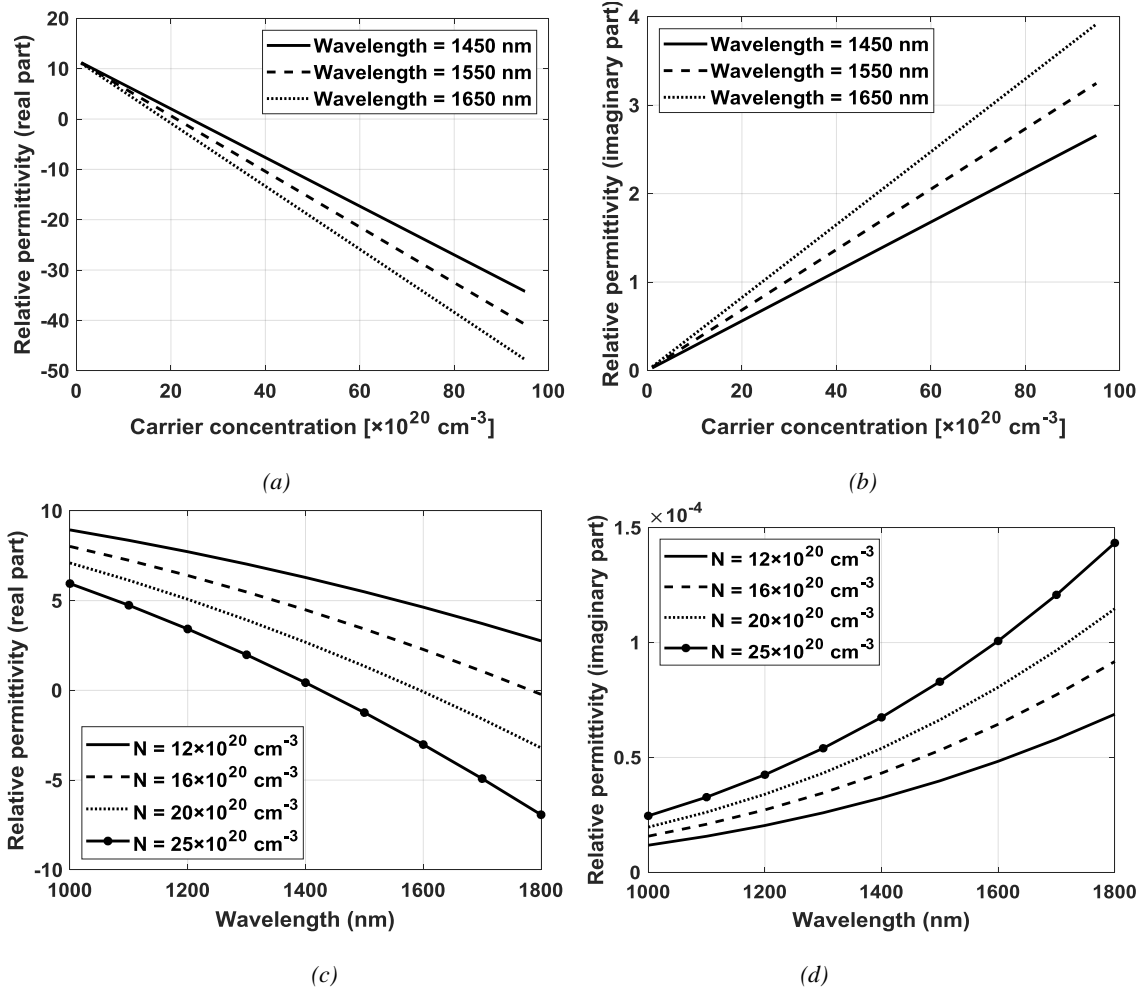

(a)

(b)

(c)

(d)

Fig 2. Relative permittivity (a) real part (b) imaginary part versus carrier concentration at different wavelengths, Relative permittivity (c) real part (d) imaginary part versus wavelength at different carrier concentrations
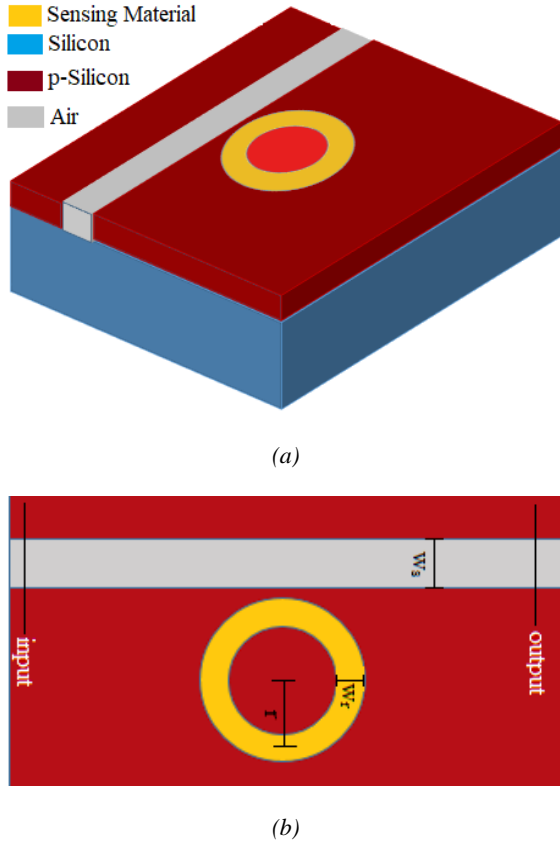
(a)

(b)

Fig. 3. (a) 3D and (b) 2D model of the proposed sensor (color online)

The basic scheme of the plasmonic sensor is composed of a straight waveguide of silicon-air-silicon structure which is coupled with a ring cavity inside the silicon layer in which there will be the material under sense. Figs. 3(a) and 3(b) show the 3D and 2D models of the sensor respectively. Here, w = 50 nm, r = 140 nm, gap = 8 nm is chosen. The height of the device also plays an important role in the performance of the device. The loss of the device decreases significantly after a certain height. Though the simulation result of most of the proposed plasmonic sensors as well as this work is simulated in 2D for an efficient simulation and lower loss [54]. For practical experiments, the result will match with the 2D simulation result for the ideal case which is h= ∞. For any height greater than 50 nm, the result will be stable and very close to the simulation result [10]. The other parameters are varied and the best one is selected.

3. Results and discussions

For the simulation purpose of this work, commercial simulation software COMSOL Multiphysics version 5.3 is used which employs Finite Element Method (FEM) with scattering boundary condition for the calculation and simulation purpose. At first, the plasmonic sensor has been analyzed by varying different design parameters like doping concentration, the width of the straight waveguide,

the width of the ring, the radius of the ring, and the gap between the straight waveguide and the ring.

Fig. 4 shows the transmission properties for different carrier concentrations of highly doped p-silicon waveguides with r = 140 nm, w = 50 nm, and gap = 8 nm. The carrier concentration is varied from 86×10^{20} cm^{-3} to 94×10^{20} cm^{-3} and the transmission property is analyzed. The transmission property shows that the resonant wavelength performs a blue shift if the carrier concentration is increased. This resonant wavelength can be tuned depending on the application requirement by varying the carrier concentration. The sensitivity of the device is also calculated for different carrier concentration which is given by,

$$S = \frac{\Delta\lambda}{\Delta n} \quad (4)$$

where S is the sensitivity, $\Delta\lambda$ is the resonant wavelength shift and Δn is the change of refractive index. Fig. 5 shows the plot of sensitivity against different carrier concentrations.

The Figure of Merit (FOM) and Detection Limit (DL) are other key parameters to evaluate the performance of the sensors. FOM is the ratio\ of Sensitivity and Full width at half maximum (FWHM) which can be expressed by the equation,

$$FOM = \frac{S}{FWHM} \quad (5)$$

The Detection limit can be calculated using the formula,

$$DL = \Delta n \times \frac{\Delta\lambda_{min}}{\Delta\lambda_{peak}} \quad (6)$$

where Δn is the change of refractive index, $\Delta\lambda_{min}$ is the minimum resolution of the optical spectrum analyzer, and $\Delta\lambda_{peak}$ is the resonant peak shift. If a high-resolution spectrum analyzer is used, the value of $\Delta\lambda_{min}$ can be considered to be 0.001 nm.

Here, a carrier concentration of 90×10^{20} cm^{-3} is used for calculations. Similarly, the other parameters like the width of the straight waveguide, ws, the width of the ring, wr, the radius of the ring, r and the coupling gap, g, between the straight waveguide and the ring is varied and the sensitivity is calculated for n = 1 and n = 1.005. The plot of the sensitivity vs different parameters is shown in Fig. 6.
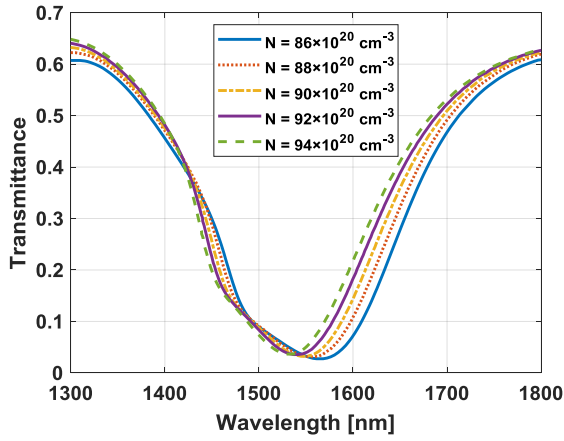
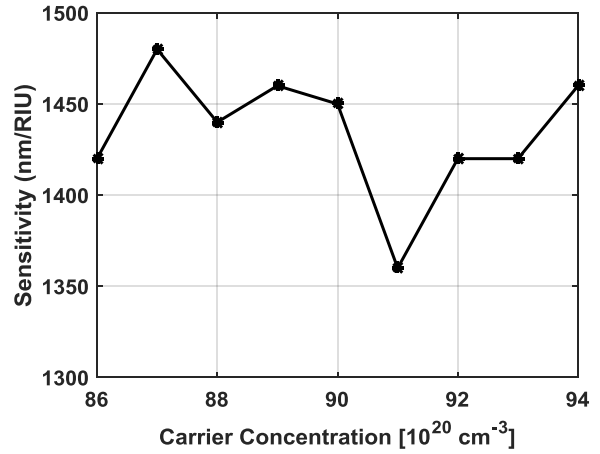*Fig. 4. Transmission properties for different carrier concentrations of highly doped p-silicon (color online)*

Fig. 5. A Plot of sensitivity against different carrier concentrations for the proposed sensor
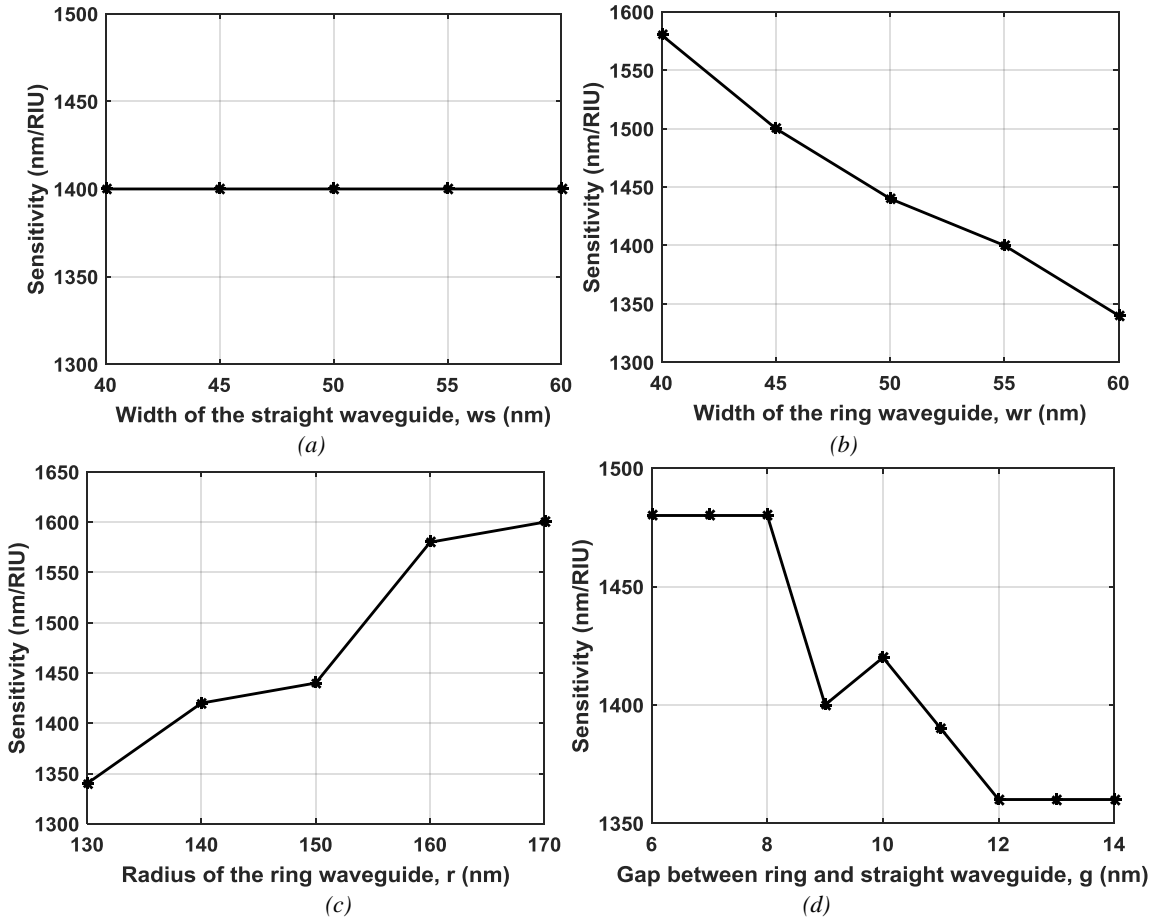

Fig.6. The plot of sensitivity against (a) width of the straight waveguide, ws, (b) width of the ring waveguide, wr, (c) radius of the ring waveguide, r, and (d) gap between the straight and ring waveguide, g

Analyzing the simulation results, the values of the different parameters of the device are selected as ws = 50 nm, wr = 50 nm, r = 170 nm, and gap = 8 nm for obtaining the maximum sensitivity of the device. Finally, the sensitivity of the device is calculated for the selected parameters by varying the value of n within a range of n = 1 to n = 1.03 taking Δn = 0.005.

The plot of transmittance vs wavelength is shown in Fig. 7. From the plot, the resonance shift can be calculated which is shown in Fig. 8, and from the resonance shift, the sensitivity is calculated.
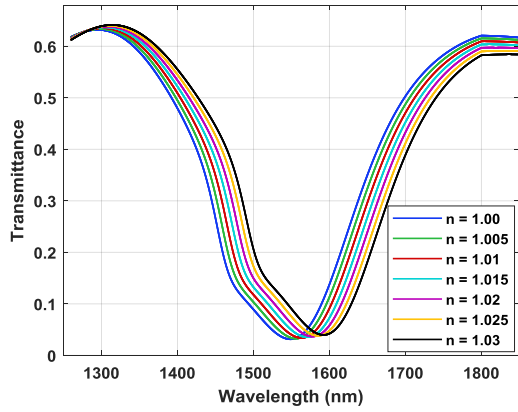
Fig. 7. The plot of transmittance vs wavelength taking Δn = 0.005 for the proposed sensor (color online)

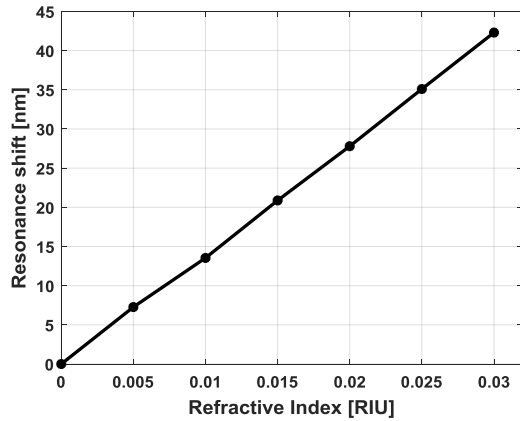*Fig. 8. Resonance shift for Δn = 0.005*

The sensitivity of the devices is obtained as 1434 nm/RIU, 1254 nm/RIU, 1468 nm/RIU, 1384 nm/RIU, 1500 nm/RIU, 1460 nm/RIU, and 1440 nm/RIU for refractive index values 1, 1.005, 1.01, 1.015, 1.02, 1.025, 1.03 respectively. Thus, the maximum sensitivity of the device is obtained as 1500 nm/RIU. However, the maximum FOM obtained here is comparatively low (≈ 7). Thus, an improvement in the FOM value is necessary to make it more efficient in sensing applications. To improve the FOM value, the FWHM of the resonance dip should be smaller. To realize it, the carrier concentration in doped silicon is increased further and the obtained improvement in results in terms of FOM and Sensitivity is shown in Table 1.

Table 1. The Sensitivity and the FOM of the sensor for different carrier concentrations of doped silicon

Carrier Concentration (10^{20} cm^{-3})	Peak for n=1 (nm)	Peak for n= 1.012 (nm)	Sensitivity (nm/RIU)	FWHM (nm)	FOM
90	1532	1545.44	1344	175.3	7.67
100	1495	1509	1400	156.22	8.96
110	1462	1477	1500	152.24	9.85
120	1432	1447.3	1530	137.34	11.14
130	1408	1424	1600	130.91	12.22
140	1386	1403	1700	117.74	14.44
150	1372.5	1394	2150	114.22	18.86

From Table 1, it is observed that with the increase in carrier concentration of doped silicon, both the sensitivity and FOM of the device increases. Here, the highest sensitivity obtained is 2150 nm/RIU and the highest FOM obtained is 18.86. The transmission characteristics for n = 1 to n = 1.03 taking Δn = 0.005 for doping concentration, N = 150×10^{20} cm^{-3} are depicted in Fig. 9. The transmission characteristics is for n = 1 to n = 1.03 is depicted in Fig. 9. The FHWM of the resonance dip has now become smaller and the resultant FOM value has increased from 7.67 to 18.86. The results obtained here can be further improved by increasing the carrier concentration in doped silicon. However, achieving a high doping concentration in silicon is still a challenge. Thus, the doping concentration level in silicon should be carefully chosen depending on applications and available technology.
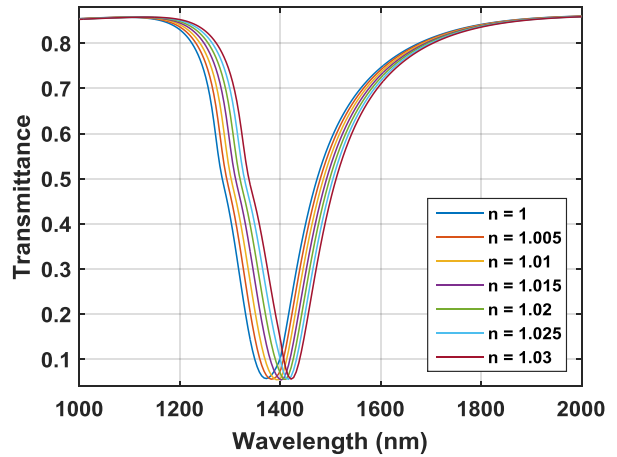

Fig. 9. The plot of transmittance vs wavelength taking Δn = 0.005 for the proposed sensor (color online)

The detection limit (DL) of the sensor is calculated using equation (6) and the value obtained was 4.65×10^{-7} RIU. The detection limit obtained here is smaller than most of the sensors. The obtained FOM is still lower compared to the MIM waveguide sensors. However, considering higher sensitivity and smaller DL values, the sensor performance is better than most of the sensors reported to date.

A comparison is shown between the proposed sensor and the state-of-the-art in Table 2. Most of the sensors are based on the metal-insulator-metal structure. Although some of the proposed sensors have a higher sensitivity and FOM compared to the sensor proposed here, those are of much more complex structures compared to the simple design proposed here. Moreover, the sensor proposed here is designed with a CMOS compatible material and hence offers a significant contribution considering the practical fabrication of the device. The sensitivity obtained here is also comparable with most of the proposed sensors and can be considered for on-chip sensing applications.

Table 2. Comparison with other proposed sensors

	Maximum Sensitivity (nm/RIU)	CMOS Compatibility	Year	FOM	DL (RIU)
This work	2150	Yes	2021	18.86	4.65×10^{-7}
Xiao et al. [55]	840	No	2021	3.9×10^5	1.19×10^{-6}
Butt et al. [56]	1320	No	2021	16.7	7.56×10^{-7}
Mahmud et al. [57]	2325	No	2021	46	4.30×10^{-6}
Jumat et al. [58]	3400	No	2021	36	2.94×10^{-7}
Butt et al. [59]	2300	No	2020	31.5	4.34×10^{-7}
Kazanskiy et al. [60]	1084.21	No	2020	57.06	9.23×10^{-7}
Butt et al. [61]	1948.67	No	2020	32.86	5.13×10^{-7}
Asgari et al.[62]	1270	No	2020	58	7.87×10^{-7}
Amoosoltani et al. [63]	1500	No	2020	242.66	6.67×10^{-7}

4. Fabrication techniques and tolerance analysis

The main advantage of the device presented here is that it can be fabricated in a similar way to the SOI devices. The sensor structure can be formed on an SOI wafer with a silicon core. The width of the silicon core can be 240 nm as SOI wafers with 220 nm thick silicon layers are one of the most widely used platforms. However, it may vary depending on applications and available techniques. The sensor structure can be patterned using both Plasma-assisted CVD and Electron-beam lithography. Electron-beam lithography can draw custom patterns with sub-10nm resolution which is an advantage of this method. Thus, it can produce devices of high resolution. To form the waveguides deep reactive-ion etching can be used. Lastly, the Ion implantation method can be used to heavily dope the silicon structure with boron impurities. However, any inaccuracy during the fabrication process like a dimensional mismatch, non-uniform structure, etc. may affect the performance of the device. To analyze the effects of such inaccuracy, several such cases are studied here.
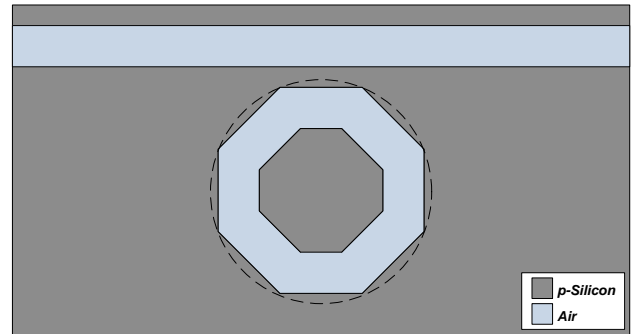

Fig. 10. Deformation of the circular ring due to fabrication inaccuracy (color online)

Fig. 10 shows the irregularity during fabrication of the circular ring waveguide. Instead of a perfect circle, structures similar to polygons may be formed in both the inner and the outer sides of the ring waveguide due to fabrication inaccuracy and the performance of the device may be affected. These effects are analyzed and shown in Table 3.

Table 3. Analysis of the change in device sensitivity due to inaccuracy in ring waveguide fabrication

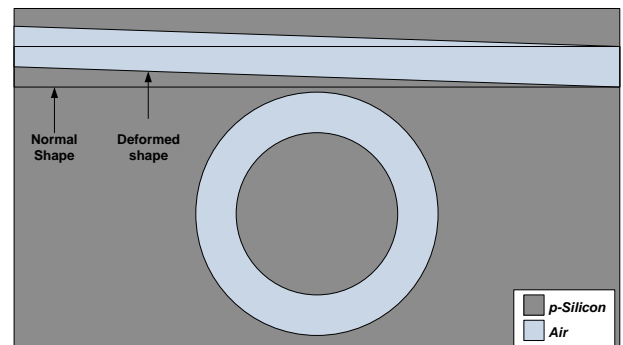| Deformed Shape of the ring waveguide	Sensitivity (nm/RIU)	Change in Sensitivity (%)
Circular	2150	---
Inner ring octagonal	2050	-4.65
Outer ring octagonal	2000	-6.97
Both ring octagonal	2030	-5.58

Fig. 11. Asymmetric gap between the ring and straight waveguide due to the rotation of the straight waveguide (color online)

The gap between the straight waveguide and the ring may become asymmetric if the straight waveguide is rotated left or right by a certain angle as depicted in Fig. 11. The effects of this rotation on the device performance are shown in Table 4.

Table 4. Analysis of the change in device sensitivity due to the rotation of the straight waveguide

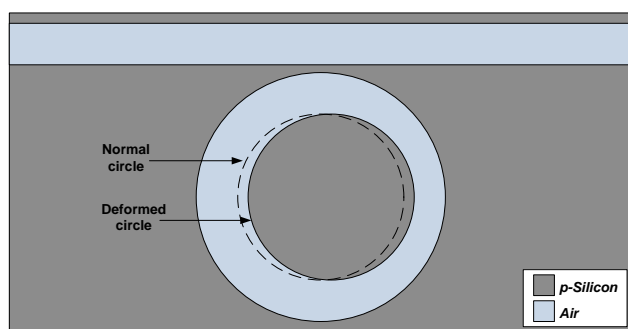| Waveguide rotation	Sensitivity (nm/RIU)	Change in Sensitivity (%)
0°	2150	---
+5°	2160	0.46
-5°	2160	0.46

Fig. 12. Non-uniform width of the ring waveguide due to fabrication inaccuracy (color online)

The sensitivity of the device will get affected if the width of the ring waveguide becomes non-uniform as depicted in Fig. 12 during fabrication. This effect can be analyzed by moving the inner circle in any direction by a small margin. The results are summarized in Table 5.

Table 5. Analysis of the change in device sensitivity due to non-uniformity of the ring width

Inner ring shift (nm)	Sensitivity (nm/RIU)	Change in Sensitivity (%)
0	2150	---
+2	2230	3.72
-2	2000	-6.97
+4	2320	7.91
-4	1952	-9.21

From the analyses of the three cases, it is observed that the effect of the fabrication inaccuracy on the device performance is less than 10%. The minimum sensitivity obtained here is 1950 nm/RIU which is still high. The sensitivity even increases in some cases. Thus, we can conclude that the device reported here has got a high level of fabrication tolerance.

5. Conclusions

A plasmonic sensor based on a highly doped silicon waveguide is proposed and analyzed here that uses heavily doped silicon as the plasmonic material, unlike the traditional MIM waveguide. The sensitivity of the proposed sensor is as high as 2150 nm/RIU which is large enough for practical applications as a refractive index sensor. The detection limit of the sensor is also as small as 4.65×10^{-7} RIU. The only limitation of the proposed sensor is in terms of a lower FOM value of 18.86 which can be further improved. Moreover, its simple framework, high fabrication tolerance and, all-silicon approach make it CMOS compatible and thus provide an easier and more practical way of fabrication.

References

[1] W. L. Barnes, A. Dereux, T. W. Ebbesen, Nature **424**(6950), 824 (2003).
[2] H. Lu, X. Liu, G. Wang, D. Mao, Nanotechnology **23**(44), 444003 (2012).
[3] H. Wang, J. Yang, J. Zhang, J. Huang, W. Wu, D. Chen, and G. Xiao, Opt. Lett. **41**(6), 1233 (2016).
[4] J. Tian, S. Yu, W. Yan, M. Qiu, Appl. Phys. Lett. **95**(1), 13504 (2009).
[5] S. Bahadori-Haghighi, R. Ghayour, M. H. Sheikhi, Plasmonics **129**(4), 653 (2018).
[6] N. Gogoi, P. P. Sahu, Appl. Opt. **57**(10), 2715 (2018).
[7] N. Nozhat, N. Granpayeh, Opt. Commun. **284**(13), 3449 (2011).
[8] Y. Guo, L. Yan, W. Pan, B. Luo, K. Wen, Z. Guo, H. Li, and X. Luo, Opt. Express **19**(15), 13831 (2011).
[9] Y. Zhang, Y. Kuang, Z. Zhang, Y. Tang, J. Han, R. Wang, J. Cui, Y. Hou, W. Liu, Appl. Phys. A **125**(1), 13 (2019).
[10] Z. Zhang, J. Yang, X. He, J. Zhang, J. Huang, D. Chen, Y. Han, Sensors **18**(1), 116 (2018).
[11] M. A. Butt, S. N. Khonina, N. L. Kazanskiy, J. Mod. Opt. **65**(9), 1135 (2018).
[12] Y. Shen, J. Zhou, T. Liu, Y. Tao, R. Jiang, M. Liu, G. Xiao, J. Zhu, Z. Zhou, X. Wang, C. Jin, J. Wang, Nat. Commun. **4**, 2381 (2013).
[13] H. Wang, Sci. Rep. **8**(1), 9589 (2018).
[14] S. A. Maier, Plasmonics: fundamentals and applications. Springer Science & Business Media, 2007.
[15] T. Wu, Y. Liu, Z. Yu, Y. Peng, C. Shu, H. Ye, Opt. Express **22**(7), 7669 (2014).
[16] T. Srivastava, R. Das, R. Jha, Plasmonics **8**(2), 515 (2013).
[17] M. Y. Azab, M. F. O. Hameed, S. S. A. Obayya, Computational Photonic Sensors, Springer, 179 (2019).
[18] A. Tittl, H. Giessen, N. Liu, Nanophotonics **3**(3), 157 (2014).
[19] J. M. Bingham, J. N. Anker, L. E. Kreno, R. P. Van Duyne, J. Am. Chem. Soc. **132**(49), 17358 (2010).
[20] A. G. Brolo, Nat. Photonics **6**(11), 709 (2012).
[21] W. Law, K. Yong, A. Baev, P. N. Prasad, ACS Nano **5**(6), 4858 (2011).
[22] P. B. Johnson, R.-W. Christy, Phys. Rev. B **6**(12), 4370 (1972).
[23] P. R. West, S. Ishii, G. V Naik, N. K. Emani, V. M. Shalaev, A. Boltasseva, Laser Photon. Rev. **4**(6), 795 (2010).

[24] A. V. Kildishev, V. M. Shalaev, Opt. Lett. **33**(1), 43 (2008).

[25] W. Cai, U. K. Chettiar, A. V. Kildishev, V. M. Shalaev, Nat. Photonics **1**(4), 224 (2007).

[26] Y. Yagil, G. Deutscher, Thin Solid Films **152**(3), 465 (1987).

[27] F. Abelès, Y. Borensztein, T. López-Rios, Advances in Solid State Physics, Springer, 93 (1984).

[28] V. B. Berestetskii, L. D. Landau, E. M. Lifshitz, L. P. Pitaevskii, Quantum electrodynamics, **4**, Butterworth-Heinemann, 1982.

[29] G. V. Naik, V. M. Shalaev, A. Boltasseva, Adv. Mater. **25**(24), 3264 (2013).

[30] E. D. Palik, Handbook of Optical Constants of Solids, Five-Volume Set: Handbook of Thermo-Optic Coefficients of Optical Materials with Applications. Elsevier, 1997.

[31] M. G. Saber, N. Abadía, Y. Wang, D. V Plant, Opt. Commun. **415**, 121 (2018).

[32] Y. A. Vlasov, IEEE Commun. Mag. **50**(2), s67 (2012).

[33] X. Chen, M. M. Milosevic, S. Stanković, S. Reynolds, T. D. Bucio, K. Li, D. J. Thomson, F. Gardes, G. T. Reed Proc. IEEE **106**(12), 2101(2018).

[34] M. G. Saber, G. Vall-Llosera, D. Patel, A. Samani, R. Li, M. Morsy-Osman, M. Chagnon, E. El-Fiky, R. Gutiérrez-Castrejón, P. J. Urban, B. Dortschy, F. Cavaliere, S. Lessard, D. V. Plant,, Opt. Commun. **450**, 48 (2019).

[35] M. G. Saber, L. Xu, R. H. Sagor, Y. Wang, A. Kumar, D. Mao, E. El-Fiky, D. Patel, A. Samani, Z. Xing, M. Jacques, Y. D'Mello, D. V. Plant1, IET Optoelectron. **14**(3), 109 (2020).

[36] D. Thomson, A. Zilkie, J. E. Bowers, T. Komljenovic, G. T. Reed, L. Vivien, D. Marris-Morini, E. Cassan, L. Virot, J. Fédéli, J. Hartmann, J. H. Schmid, D. Xu, F. Boeuf, P. O'Brien, G. Z. Mashanovich, M. Nedeljkovic, J. Opt. **18**(7), 73003 (2016).

[37] M. G. Saber, D. V. Plant, N. Abadía, AIP Adv. **11**(4), 045219 (2021).

[38] C. Doerr, L. Chen, Proc. IEEE **106**(12), 2291 (2018).

[39] A. Katumba, X. Yin, J. Dambre, P. Bienstman, J. Light. Technol. **37**(10), 2232 (2019).

[40] X. Zhang, Y. Qi, P. Zhou, H. Gong, B. Hu, C. Yan, Photonic Sensors **8**(4), 367 (2018).

[41] M. G. Saber, N. Abadía, D. V Plant, Opt. Express **26**(16), 20878 (2018).

[42] M. Shahzad, G. Medhi, R. E. Peale, W. R. Buchwald, J. W. Cleary, R. Soref, G. D. Boreman, O. Edwards., J. Appl. Phys. **110**(12), 123105 (2011).

[43] D. Linaschke, N. Schilling, I. Dani, U. Klotzbach, C. Leyens, Energy Procedia **55**, 247 (2014).

[44] I. Mizushima, A. Murakoshi, M. Watanabe, M. Yoshiki, M. Hotta, M. Kashiwagi, Jpn. J. Appl. Phys. **33**(1S), 404 (1994).

[45] L. Vina, M. Cardona, Phys. Rev. B **29**(12), 6739 (1984).

[46] Z. Ma, Y. Liu, L. Deng, M. Zhang, S. Zhang, J. Ma, P. Song, Q. Liu, A. Ji, F. Yang, X. Wang, Nanomaterials **8**(2), 77 (2018).

[47] M. Miyao, T. Motooka, N. Natsuaki, T. Tokuyama, Solid State Commun. **37**(7), 605 (1981).

[48] G. E. Jellison Jr, F. A. Modine, C. W. White, R. F. Wood, R. T. Young, Phys. Rev. Lett. **46**(21), 1414 (1981).

[49] D. Nobili, S. Solmi, A. Parisini, M. Derdour, A. Armigliato, L. Moro, Phys. Rev. B **49**(4), 2477 (1994).

[50] Z. Qi, G. Hu, L. Li, B. Yun, R. Zhang, Y. Cui, IEEE Photonics J. **8**(3), 1 (2016).

[51] Y.-B. Chen, Z. M. Zhang, J. Phys. D. Appl. Phys. **41**(9), 95406 (2008).

[52] D. K. Schroder, R. N. Thomas, J. C. Swartz, IEEE J. Solid-State Circuits **13**(1), 180 (1978).

[53] M. Van Exter, D. Grischkowsky, Phys. Rev. B **41**(17), 12140 (1990).

[54] S. Naghizadeh, Ş. E. Kocabaş, J. Opt. Soc. Am. B **34**(1), 207 (2017).

[55] G. Xiao, Y. Xu, H. Yang, Z. Ou, J. Chen, H. Li, X. Liu, L. Zeng, J. Li, Sensors **21**(4), 1 (2021).

[56] M. A. Butt, S. N. Khonina, N. L. Kazanskiy, Waves in Random and Complex Media **31**(1), 146 (2021).

[57] R. Al Mahmud, M. O. Faruque, R. H. Sagor, Plasmonics, **16**(3), 873(2021).

[58] S. Zubaidah binti Haji Jumat et al., Chinese J. Phys. **71**, 286 (2021).

[59] M. A. Butt, N. L. Kazanskiy, S. N. Khonina, Photonic Sensors **10**(3), 223 (2020).

[60] N. L. Kazanskiy, M. A. Butt, S. N. Khonina, Photonics Nanostructures - Fundam. Appl. **42**, 100836 (2020).

[61] M. A. Butt, N. L. Kazanskiy, S. N. Khonina, Curr. Appl. Phys. **20**(11), 1274 (2020).

[62] S. Asgari, S. Pooretemad, N. Granpayeh, Photonics Nanostructures - Fundam. Appl. **42**, 100857 (2020).

[63] N. Amoosoltani, N. Yasrebi, A. Farmani, A. Zarifkar, IEEE Sens. J. **20**(16), 9097 (2020).

_____

*Corresponding author: omarfaruque@iut-dhaka.edu